



# The effect of sulfur dioxide on the activity of hierarchical Pd-based catalysts in methane combustion

Matteo Monai<sup>a</sup>, Tiziano Montini<sup>a</sup>, Michele Melchionna<sup>a</sup>, Tomáš Duchoň<sup>b</sup>, Peter Kúš<sup>b</sup>, Chen Chen<sup>c</sup>, Nataliya Tsud<sup>b</sup>, Lucia Nasi<sup>d</sup>, Kevin C. Prince<sup>e,f</sup>, Kateřina Veltruská<sup>b</sup>, Vladimír Matolín<sup>b</sup>, Mahmoud M. Khader<sup>g</sup>, Raymond J. Gorte<sup>c</sup>, Paolo Fornasiero<sup>a,\*</sup>

<sup>a</sup> Department of Chemical and Pharmaceutical Sciences, ICCOM-CNR URT Trieste, Consortium INSTM Trieste Research Unit, University of Trieste, via L. Giorgieri 1, 34127 Trieste, Italy

<sup>b</sup> Charles University, Faculty of Mathematics and Physics, Department of Surface and Plasma Science, V Holešovičkách 2, 18000 Prague, Czech Republic

<sup>c</sup> Department of Chemical and Biomolecular Engineering, University of Pennsylvania, 311A Towne Building, 220 South 33rd Street, Philadelphia, USA

<sup>d</sup> CNR-IMEM Institute, Parco area delle Scienze 37/A, 43124 Parma, Italy

<sup>e</sup> Elettra-Sincrotrone Trieste SCpA, Strada Statale 14, km 163.5, 34149 Basovizza, Trieste, Italy

<sup>f</sup> IOM, Strada Statale 14, km 163.5, 34149 Basovizza, Trieste, Italy

<sup>g</sup> Gas Processing Center, College of Engineering, Qatar University, Doha, P.O. Box 2713, Qatar

## ARTICLE INFO

### Article history:

Received 31 August 2016

Accepted 5 September 2016

Available online 5 September 2016

### Keywords:

Sulfur dioxide

Methane oxidation catalysts

Palladium

Ceria-Zirconia

XPS

## ABSTRACT

SO<sub>2</sub> poisoning of methane oxidation over alumina-supported, Pd@Ce<sub>x</sub>Zr<sub>1-x</sub>O<sub>2</sub> nanoparticle catalysts was systematically studied by means of advanced PhotoElectron Spectroscopy (PES) methods. The Pd@Ce<sub>x</sub>Zr<sub>1-x</sub>O<sub>2</sub> units were synthesized and deposited on two modified-alumina supports, i.e. high surface area modified alumina and a model alumina prepared by Atomic Layer Deposition (ALD) of alumina on Indium Tin Oxide (ITO)/quartz slides. The model support was designed to be suitable for PES analysis and was stable to high temperature treatments (850 °C). Characterization of the high-surface-area (HSA) catalysts by X-Ray Diffraction (XRD), N<sub>2</sub> physisorption, CO chemisorption and Transmission Electron Microscopy (TEM) indicated formation of CeO<sub>2</sub>-ZrO<sub>2</sub> (CZ) mixed-oxide crystallites that stabilize the Pd active phase against sintering. Correlation of methane-oxidation rates with PES results demonstrated two distinct mechanisms for deactivation by SO<sub>2</sub>. Below 450 °C, the presence of SO<sub>2</sub> in the feed led to partial reduction of the active PdO phase and to the formation of sulfates on the Pd. Above 500 °C, poisoning by SO<sub>2</sub> was less severe due to spillover of the sulfates onto the oxide promoter. Pd@ZrO<sub>2</sub> catalysts showed the best resistance to SO<sub>2</sub> poisoning, outperforming analogous Pd@CZ mixed-oxide catalysts, because there was less sulfate formation and the sulfates that did form could be removed during regeneration.

© 2016 Elsevier B.V. All rights reserved.

## 1. Introduction

Regulations for automotive emissions are becoming more stringent in order to mitigate the effects of transportation on air quality, environment and human health. Electric vehicles and hydrogen-powered, fuel-cell cars may solve these problems in the future, but hydrocarbon fuels will continue to be used in the near term. Because of fuel availability and improved efficiency, there will likely be a move towards more Natural Gas Vehicles (NGVs) and diesel-powered cars; but these both have the disadvantage that methane, a greenhouse gas, is present in significant amounts in

their exhausts. This represents a serious challenge for complying with upcoming regulations. Low-temperature methane catalytic combustion is also important for gas turbines fueled with natural gas. Therefore, better methane-oxidation catalysts, with high activities at low temperatures and better stability, are needed.

Palladium-based catalysts are the most active materials for oxidation of methane at low temperatures, especially when they are promoted by the presence of reducible oxides such as CeO<sub>2</sub> [1–5]. However, they suffer from deactivation under realistic conditions, mainly because of sintering of the metal or support and because of the presence of poisons in the gas feed, including water vapor, sulfur oxides and phosphorous compounds [6–13]. SO<sub>2</sub>, which is produced by the oxidation of sulfur compounds present in fuels and in lubricating additives [14,15], is a particularly serious poison in catalytic converters. Despite the continuing reduction of sulfur in the

\* Corresponding author.

E-mail address: [pfornasiero@units.it](mailto:pfornasiero@units.it) (P. Fornasiero).

fuels (The Ultra-Low Sulfur Diesel (ULSD) regulation established a 15 ppm sulfur content for diesel fuel in 2006 [16]), long-term exposure to low concentrations of SO<sub>2</sub> is still detrimental to the catalytic activity of the exhaust after-treatment catalysts [15,17,18]. Under lean conditions and at temperatures above 200 °C, the presence of SO<sub>2</sub> in the exhaust leads to formation of sulfate species on both the support and the active phase [19,20]. One of the possible pathways for the formation of sulfates involves SO<sub>2</sub> oxidation to SO<sub>3</sub> by O<sub>2</sub> (1) and subsequent adsorption of SO<sub>3</sub> on the metal-oxide surface (2).



Alternatively, SO<sub>2</sub> may be oxidized by oxygen from the support or disproportionate to SO and SO<sub>3</sub> [21]. Formation of sulfates on supports such as alumina can also deactivate the catalyst by acting as a buffer of SO<sub>x</sub> that prevents adsorption of SO<sub>2</sub> onto the active phase during exposure to gas-phase SO<sub>2</sub> but prolongs the poisoning effect after SO<sub>2</sub> removal due to a slow decomposition of the accumulated sulfates [14,15]. With a non-sulfating support, such as SiO<sub>2</sub>, the active phase will not be protected from poisoning, leading to faster deactivation, but also to faster recovery [14].

SO<sub>2</sub> poisoning on reducible supports, CeO<sub>2</sub> and Ce<sub>x</sub>Zr<sub>1-x</sub>O<sub>2</sub>, has been widely investigated because of the importance of these oxides in catalytic converters [22–25]. It is known that ceria forms sulfates that are stable to relatively high temperatures (600 °C–700 °C) [23,26]. ZrO<sub>2</sub> forms fewer sulfates when exposed to the same conditions, and these are mostly confined to its surface [23]. However, conflicting observations have been made regarding the resistance of Ce-Zr (CZ) mixed oxides to SO<sub>2</sub> in comparison to CeO<sub>2</sub> and ZrO<sub>2</sub>. Luo et al. reported that CeO<sub>2</sub> and CZ catalysts were affected in a similar manner by SO<sub>2</sub> poisoning for both the water-gas-shift (WGS) and CO-oxidation reactions [23], while Deshmukh et al. reported enhanced resistance to poisoning for the mixed oxides [25].

In this work, we investigate the effect of SO<sub>2</sub> poisoning on methane oxidation over hierarchical Pd@Ce<sub>x</sub>Zr<sub>1-x</sub>O<sub>2</sub> catalysts supported on modified alumina. The synthesis of these materials relies on self-assembly of functional precursors to control the catalyst nanostructure and thereby maximize the active-phase/metal-oxide promoter interfacial area [27]. This feature helps stabilize the PdO active phase at high temperature and prevents sintering during thermal annealing, which in turn leads to enhanced performance. In previous work, the hierarchical catalysts consisted of Pd nanoparticles and nanosized ceria in intimate contact, deposited on HSA Si-Al<sub>2</sub>O<sub>3</sub> support (Pd@CeO<sub>2</sub>/Si-Al<sub>2</sub>O<sub>3</sub>) [11,28]. These catalysts were very active for CH<sub>4</sub> oxidation under dry conditions [28], but deactivated in the presence of water vapor due to formation of Ce hydroxides. Replacing CeO<sub>2</sub> with ZrO<sub>2</sub> significantly improved the stability and activity in the presence of 10% H<sub>2</sub>O vapor, with complete combustion achieved at 500 °C (rather than 600 °C for CeO<sub>2</sub>-based catalysts) [29]. In the present work, we modified the previously reported synthesis conditions [30] in order to achieve a range of shell compositions, from pure CeO<sub>2</sub> to pure ZrO<sub>2</sub>. We have also investigated the effect of SO<sub>2</sub> on these core-shell catalysts using X-ray photoemission spectroscopy (XPS) on model catalysts designed to closely resemble the high-surface-area materials in both surface composition and temperature treatments, while avoiding charging and low resolution problems often experienced with powdered materials [31].

## 2. Experimental

### 2.1. Catalyst synthesis

Potassium tetrachloropalladate(II) (99.95%) was purchased from ChemPUR. Sodium borohydride (98%+) was purchased from Acros Organics. Zirconium butoxide (80% in 1-butanol), cerium ammonium nitrate (CAN, 99.99%), sodium methoxide (25% in methanol), phosphoric acid (85%), 11-mercaptoundecanoic acid (MUA, 95%), 1-dodecanethiol (DT, ≥98%) dodecanoic acid (99%), triethoxy(octyl)silane (TEOS, 97.5%), and all the solvents (analytical grade) were purchased from Sigma-Aldrich. Trimethyl Aluminum (TMA) was supplied by Cambridge Nanotech together with the ALD system. The Al<sub>2</sub>O<sub>3</sub> support was kindly provided by SASOL (PURALOX TH 100/150). Prior to use, Al<sub>2</sub>O<sub>3</sub> was stabilized by calcination at 950 °C for 24 h. ITO/quartz slides were purchased from Präzisions Glas & Optik (PGS).

The hierarchical Pd@MO<sub>x</sub> (CeO<sub>2</sub>, ZrO<sub>2</sub> and Ce<sub>x</sub>Zr<sub>1-x</sub>O<sub>2</sub>) units were prepared by modifying published procedures [30]. Briefly, Pd nanoparticles protected by 11-mercaptoundecanoic acid (MUA) dispersed in THF [30], were added to a THF solution of cerium(IV) tetrakis(decyloxy) and/or zirconium butoxide, followed by the addition of a THF solution of dodecanoic acid. Typically, 10 mL of the THF solution of MUA-Pd nanoparticles (0.5 mg/mL as Pd) were slowly added to 5 mL THF solution of pre-mixed metal alkoxides, keeping the Pd:MO<sub>x</sub> molar ratio (1:5.5) constant, followed by the addition of dodecanoic acid (1 mol vs Ce + Zr) dissolved in 10 mL of THF. Hydrolysis of the metal alkoxide in the Pd-Ce/Zr solution was carried out by slowly adding up to 1.2 mL of H<sub>2</sub>O dissolved in 10 mL of THF over a period of 4 h (up to 120 mol vs Ce + Zr).

For preparation of HSA catalysts, the Pd@MO<sub>x</sub> units were adsorbed in monolayer form onto modified, hydrophobic γ-Al<sub>2</sub>O<sub>3</sub>, prepared by reaction of calcined γ-Al<sub>2</sub>O<sub>3</sub> (powdered material) with TEOS, as discussed elsewhere [28]. The Pd(1%)/MO<sub>x</sub>/Si-Al<sub>2</sub>O<sub>3</sub> catalysts were then calcined at 850 °C in air for 5 h in order to remove the organic components and to activate the catalyst [28]. For comparison, a Pd(1%)/Si-Al<sub>2</sub>O<sub>3</sub> catalyst was prepared by deposition of DT-protected Pd nanoparticles (Pd-DT NPs) on modified hydrophobic alumina and calcination at 850 °C for 5 h. The Pd-DT NPs were prepared according to a published procedure [32].

The supports for the model catalysts were prepared by ALD of Al<sub>2</sub>O<sub>3</sub> overlayers of various thicknesses (2, 5 and 10 nm) on an ITO/quartz support (flat, low-surface-area material). Both TMA and water precursors were kept at room temperature, resulting in vapor pressures of about 20 Torr and 11 Torr, respectively. The deposition chamber was maintained at 250 °C and a base pressure of 0.1 Torr, with N<sub>2</sub> flow of 20 mL min<sup>-1</sup>. The deposition steps were as follows: 1) pulse water for 0.015 s, 2) hold 5 s, 3) pulse TMA for 0.015 s, and 4) hold 5 s. The thickness of the Al<sub>2</sub>O<sub>3</sub> film increased by approximately 1 Å/cycle, so that 50 cycles were used to make a 5 nm film. The Al<sub>2</sub>O<sub>3</sub>/ITO/quartz slides were then cut into 9 × 9 mm pieces with a glass cutter and treated in freshly prepared piranha solution (concentrated H<sub>2</sub>SO<sub>4</sub> and 30% H<sub>2</sub>O<sub>2</sub> solution in a 3:1 ratio) in order to clean the surface from any impurity and increase the hydroxyl group population. The slides were washed many times with water and acetone prior to being functionalized by reaction in a diluted solution of TEOS (0.5 mL) in toluene (20 mL) for 2 days at room temperature. The Pd@MO<sub>x</sub> units were then deposited from solution onto the Si-Al<sub>2</sub>O<sub>3</sub>/ITO/quartz slides, according to a procedure described in detail elsewhere [33]. Briefly, 0.1 mL of Pd@MO<sub>x</sub> solution was deposited onto the support and rinsed with THF after 2 min to remove weakly adsorbed particles. The model catalysts were finally calcined at 850 °C in air for 5 h.

## 2.2. Catalytic measurements

Catalytic experiments on the HSA catalysts were performed in a U-shaped quartz reactor with 25 mg of catalyst sieved for grain sizes below 150  $\mu\text{m}$ . Aging treatments on model catalysts were performed in a larger U-shaped quartz reactor, using an alumina tray to hold the model-catalyst slides in place. Reactions were carried out at a total gas pressure of 1 atm, with the inlet composition controlled by varying the flow rates of  $\text{CH}_4$ ,  $\text{SO}_2$ ,  $\text{O}_2$  and Ar. The total flow rate was 83.3  $\text{mL min}^{-1}$  for the HSA catalysts ( $\text{GHSV} \approx 2 \times 10^5 \text{ mL g}^{-1} \text{ h}^{-1}$ ) and 21.3  $\text{mL min}^{-1}$  for the model catalysts setup ( $\text{GHSV} \approx 1 \times 10^6 \text{ mL g}^{-1} \text{ h}^{-1}$ , using the volume of  $\text{Pd@CeO}_2$  added to the  $\text{Al}_2\text{O}_3/\text{ITO}$ /quartz slides). Typically, 50 ppm  $\text{SO}_2$  was used during aging, in order to accelerate deactivation of the catalyst ( $\text{SO}_2$  concentrations in the exhaust feed are more typically less than 5 ppm). The heating and cooling rates in all cases were fixed at  $10^\circ\text{C min}^{-1}$ . The composition of the effluent gases was monitored on line using a mass spectrometer. For XPS/SRPES (Synchrotron Radiation Photoelectron Spectroscopy) analysis, the catalysts were rapidly cooled to room temperature under dry conditions at the end of the aging treatment and finally stored under Ar until rapid transfer to the XPS chamber.

## 2.3. Characterization techniques

The HSA catalysts were characterized by powder X-Ray Diffraction (XRD) for structural analysis,  $\text{N}_2$  physisorption for surface area measurements, CO chemisorption for metal dispersion evaluation, Transmission Electron Microscopy (TEM)/Energy Dispersive X-Ray Spectroscopy (EDS) for morphological analysis, and X-ray Photoelectron Spectroscopy (XPS) for comparison with the model catalyst.

XRD patterns were collected on a Philips X'Pert diffractometer using a monochromatized  $\text{Cu K}\alpha$  ( $\lambda = 0.154 \text{ nm}$ ) X-ray source in the range  $10^\circ < 2\theta < 100^\circ$ . Mean crystallite sizes were calculated by applying the Scherrer equation to the principal reflection of each phase.  $\text{N}_2$  physisorption experiments were carried out on a Micromeritics ASAP 2020C. The samples were first degassed in vacuum at  $350^\circ\text{C}$  for 12 h prior to  $\text{N}_2$  adsorption at liquid nitrogen temperature.

Pd accessibility was estimated by means of low temperature CO chemisorption measurements. Typically, 150 mg of sample were pre-reduced at  $80^\circ\text{C}$  under 5.0%  $\text{H}_2/\text{Ar}$  for 30 min, degassed for 30 min at  $80^\circ\text{C}$  and for 4 h at  $350^\circ\text{C}$ . The samples were then cooled to  $-80^\circ\text{C}$  using an acetone-dry ice bath and exposed to between 2 and 20 Torr of CO. Equilibrium was considered to have been reached when the pressure change was less than 0.01% for 11 consecutive readings, taken at 30-s intervals. Adsorbed volumes were determined by extrapolation of the linear part of the adsorption isotherm to zero pressure. A 1:1 CO/Pd chemisorption stoichiometry ratio was assumed.

The samples were characterized by TEM, performed on a JEOL 2200FS microscope, equipped with a High-Angle Annular-Dark-Field (HAADF) detector, in-column energy filter and EDS.

Model catalysts were characterized by XPS and SRPES for surface chemical analysis, Ion Scattering Spectroscopy (ISS) for investigating of the chemical composition of the outmost surface layer, Atomic Force Microscopy (AFM) and Scanning Electron Microscopy (SEM) for morphological analysis, and EDS for bulk chemical analysis. XPS and SRPES experiments were carried out at the Materials Science Beamline (MSB) at the Elettra Synchrotron Light Source in Trieste, Italy. The MSB is a bending magnet beamline with a plane grating monochromator that provides light in the energy range of 21–1000 eV. The UHV end station, with a base pressure of  $1 \times 10^{-8} \text{ Pa}$ , is equipped with an electron energy analyzer (Specs Phoibos 150) and a dual Mg/Al X-ray source. High-resolution SRPES

measurements were performed on the following core levels: Pd 3d (610 eV), Zr 3d (425 eV), O 1s (610 eV), C 1s (425 eV), S 2p (425 eV), Al 2p (124.8 eV) and Si 2p (150 eV). Complementary XPS spectra of Pd 3d, Ce 3d, Zr 3d, O 1s, C 1s, S 2p, Al 2p, Si 2p, Sn 3d and In 3d core levels were recorded at the same end station, using the excitation energy of 1486.6 eV (Al  $\text{K}\alpha$ ). The apparent degree of reduction of ceria was determined from the Ce 3d spectra, using the procedure described in a previous publication [34]. Binding energies are reported after correction for charging, using adventitious C 1s as a reference.

$\text{He}^+$  ions with the energy of 2 keV and the impact angle of  $45^\circ$  were used for the ISS analysis. AFM was performed using a Nanoscope V (Digital Instruments Metrology Group, model MMAFMLN) in tapping mode in air at room temperature, using an n-type silicon  $\mu\text{mash}^\circ$  SPM probe (HQ:NSC15/AL BS) with tip height of 12–18  $\mu\text{m}$  and cone angle  $<40^\circ$  (Resonant frequency 325 kHz, force constant of  $\sim 40 \text{ N m}^{-1}$ ). SEM measurements were performed on a field-emission Scanning Electron Microscope (SEM) (Model Tescan Mira 3). High resolution was achieved using an acceleration voltage of 30 kV and a working distance of less than 3 mm. A Bruker XFlash<sup>®</sup> 6 | 10 Energy Dispersive X-ray Spectrometer was used to carry out elemental mapping of the sample. Characteristic X-ray radiation was excited by 20 keV primary electrons.

## 3. Results

### 3.1. High-surface-area (HSA) catalysts

The synthesis of  $\text{Pd@CeO}_2$  and  $\text{Pd@ZrO}_2$  particles reported in previous works [28,30] was modified in this study to allow the preparation of  $\text{Pd@Ce}_x\text{Zr}_{1-x}\text{O}_2$  particles. Ce and Zr alkoxides were mixed together before slowly adding the dispersed Pd-MUA nanoparticles to allow the reaction of both alkoxides with the carboxylic group of MUA. The Pd:(Ce+Zr) molar ratio was kept constant and the following Ce:Zr molar ratios were selected to investigate the generality of the synthetic method: (80:20), (60:40), (40:60), (20:80). Pure  $\text{Pd@CeO}_2$  and  $\text{Pd@ZrO}_2$  units were also prepared as references. After controlled hydrolysis, the particles were deposited on hydrophobic, silanized alumina and the materials were calcined at  $850^\circ\text{C}$  for 5 h. The final  $\text{Pd@MO}_x/\text{Si-Al}_2\text{O}_3$  catalysts were characterized by XRD to check for the formation of mixed or segregated CZ oxide phases (Figs. 1, S1 for total XRD pattern).

A complete Rietveld analysis of the CZ XRD pattern was not possible due to overlap with the signal from the  $\text{Al}_2\text{O}_3$  support, which was more than 90 wt% of the studied materials and consisted of a mixture of metastable  $\gamma$ - and  $\theta$ - $\text{Al}_2\text{O}_3$  after thermal pre-treatment [35]. Nonetheless, the partial XRD spectrum reported in Fig. 1 clearly showed the first and most intense reflection of the CZ mixed oxides, which varied between  $28.5^\circ$  (for  $\text{CeO}_2$ ) to  $30.2^\circ$  (for  $\text{ZrO}_2$ ). Therefore, only pseudo-cubic cell parameters were calculated in the present case, despite the fact that a transition from cubic to tetragonal crystal structure is expected in the oxide promoter with high  $\text{ZrO}_2$  content [36]. The linear dependence of the cell parameter for the pseudo-cubic cells with the CZ composition is consistent with the formation of solid solutions between  $\text{CeO}_2$  and  $\text{ZrO}_2$  (inset of Fig. 1) [37]. Only in the case of CZ 40:60 a shoulder appeared at lower diffraction angles, suggesting that segregation of a small amount of a  $\text{CeO}_2$ -rich phase occurred for that sample. Phase separation has been observed previously for CZ mixed oxides with 40:60 Ce:Zr ratios, because this composition is thermodynamically unstable [36]. The decreased intensity of the main reflection with increasing  $\text{ZrO}_2$  content is due to the lower weight loading and scattering factor of Zr.

The mean crystallite sizes of the CZ mixed oxides were calculated to be in the range of 7–11 nm (Table S1 in the Supplementary



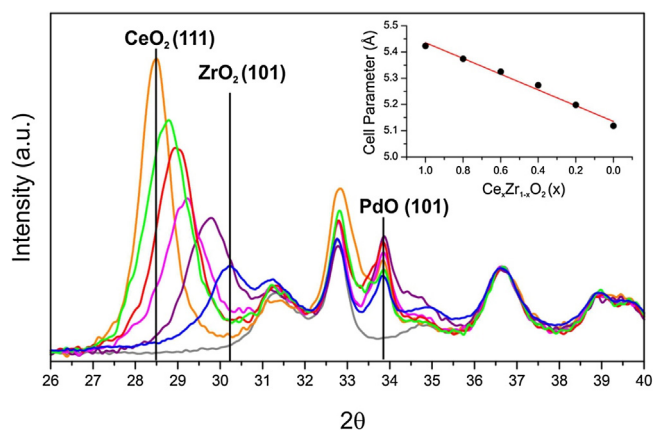


**Fig. 1.** XRD patterns of the Si-Al<sub>2</sub>O<sub>3</sub> calcined at 850 °C for 5 h (grey line) and Pd@MO<sub>x</sub>/Si-Al<sub>2</sub>O<sub>3</sub> samples calcined at 850 °C for 5 h (orange: CeO<sub>2</sub>; green: CZ 80:20; red: CZ 60:40; magenta: CZ 40:60; purple: CZ 20:80; blue: ZrO<sub>2</sub>). (For interpretation of the references to colour in this figure legend, the reader is referred to the web version of this article.)

information), which is in good agreement with TEM results (5–10 nm apparent particles size). Notably, the apparent size of CZ mixed-oxide crystallites is smaller than that of CeO<sub>2</sub>, as expected in view of the stabilizing effect of Zr [37]. The most intense reflection for PdO, the (101) plane, can be observed at 34°. The fitting of this line is complicated by the overlapping of other reflections, so that the mean crystallite size calculated by the Scherrer equation (15–18 nm, see Table S1 in the Supplementary information) is not very indicative of the actual size distribution of the PdO active phase in the samples, as discussed further in the section on TEM analysis.

Physisorption and chemisorption experiments on Pd@MO<sub>x</sub>/Si-Al<sub>2</sub>O<sub>3</sub> catalysts revealed that all the samples had similar surface areas, pore-size distributions, and Pd accessibility, as detailed in Table S2 in the Supplementary information. The results are comparable with those reported in previous studies on Pd@CeO<sub>x</sub>/Si-Al<sub>2</sub>O<sub>3</sub> and Pd@ZrO<sub>x</sub>/Si-Al<sub>2</sub>O<sub>3</sub> [11,29]. On the other hand, the Pd dispersion for the Pd/Si-Al<sub>2</sub>O<sub>3</sub> was significantly lower due to severe sintering of Pd nanoparticles. The pore-size distributions were also consistent with previous results: Pd/Si-Al<sub>2</sub>O<sub>3</sub> and the Si-Al<sub>2</sub>O<sub>3</sub> support have similar pore structures, with pore sizes in the range from 10 to 50 nm in diameter, while the Pd@MO<sub>x</sub>/Si-Al<sub>2</sub>O<sub>3</sub> catalysts exhibited fewer large pores due to partial filling with the nanostructured units, along with the formation of small pores (around 10 nm in diameter) associated with the units themselves (Fig. S2 in the Supplementary information).

Representative TEM-EDS results Fig. 2, demonstrated that all Pd@MO<sub>x</sub>-based catalysts have similar morphologies: the CZ particles, identified by EDS spectra and lattice fringes, are 5–10 nm in diameter and are sometimes aggregated. For Pd@CZ 60:40, the signals of Ce and Zr observed in EDS mapping mode are always associated and the signal analysis in spot mode revealed a good agreement with the desired Ce:Zr stoichiometric ratio. The Pd signal in EDS is typically low and diffuse, though some large palladium particles were observed, similar to what was reported by Zhang et al. for similar catalysts [38]. Such a bimodal particle distribution is not detected by XRD, since the very small PdO nanoparticles will give a broad reflection that is hard to distinguish in the presence of overlapping XRD patterns from the Al<sub>2</sub>O<sub>3</sub> support. The Pd/Si-Al<sub>2</sub>O<sub>3</sub> catalyst showed only very large Pd particles (up to 100 nm in diameter) due to severe sintering after calcination at 850 °C for 5 h. In all cases, no apparent changes in morphology were observed after any SO<sub>2</sub> aging treatments, discussed in the following section (Fig. S3 in the Supplementary information).

Methane-oxidation, light-off experiments performed on each of the Pd@MO<sub>x</sub>-based catalysts showed comparable results that were similar to those previously reported for the single-oxide catalysts (Fig. S4 in the Supplementary information) [28,30]. By comparison, the Pd/Si-Al<sub>2</sub>O<sub>3</sub> catalyst showed a higher light off temperature and the usual conversion hysteresis after heating to high temperature (Fig. S4 in the Supplementary information). While light-off curves were comparable for all Pd@MO<sub>x</sub> catalysts, sulfur tolerance was expected to vary more strongly with composition. In order to study SO<sub>2</sub>-poisoning resistance, aging tests were performed in which the catalysts were exposed to specified concentrations of SO<sub>2</sub> (typically 50 ppm) at different temperatures (from 300 to 600 °C). Introducing 50 ppm of SO<sub>2</sub> into the feed under dry conditions (0.5% CH<sub>4</sub>; 2% O<sub>2</sub>; Ar balance) caused complete and irreversible deactivation of all the studied catalysts between 300 °C and 400 °C (Fig. 3). At 450 °C, each of the hierarchical, core-shell catalysts was partially regenerated under dry conditions, recovering 50–60% of their initial conversion. The final conversion trend was Pd@ZrO<sub>2</sub>/Al<sub>2</sub>O<sub>3</sub> > Pd@Ce<sub>0.6</sub>Zr<sub>0.4</sub>O<sub>2</sub>/Al<sub>2</sub>O<sub>3</sub> > Pd@CeO<sub>2</sub>/Al<sub>2</sub>O<sub>3</sub>. Although less active, the Pd/Si-Al<sub>2</sub>O<sub>3</sub> catalyst was almost completely regenerated under dry conditions. This observation suggests that the promoting effect of the metal oxides in the hierarchical catalysts is largely suppressed by SO<sub>2</sub> at 450 °C, while the active phase can be largely regenerated.

To look for longer-term effects, the methane conversions under dry conditions at 500 °C were monitored over each of the catalysts for 2 h during SO<sub>2</sub> exposure (Fig. 4A). The hierarchical catalysts deactivated sharply during the first hour of treatment, reaching a plateau at around 60% of the initial conversion. The Pd@ZrO<sub>2</sub> and Pd@CZ catalysts showed similar deactivation trends and were partially reactivated over time after reaching that plateau. The Pd@CeO<sub>2</sub> underwent a slightly slower deactivation but was not reactivated after reaching the plateau. Aging at 500 °C using different SO<sub>2</sub> concentrations resulted in different deactivation rates but did not significantly change the plateau conversion (Fig. S5 in the Supplementary information). The residual conversion is likely associated with the partially poisoned Pd phase, unpromoted by the metal oxide. Indeed, the Pd/Si-Al<sub>2</sub>O<sub>3</sub> sample was very stable under SO<sub>2</sub> aging at 500 °C, indicating that the SO<sub>2</sub> effect on Pd is largely inhibited at this temperature. Moreover, MO<sub>x</sub>/Si-Al<sub>2</sub>O<sub>3</sub> catalysts without Pd in their formulation, prepared following a similar procedure as that used to synthesize the hierarchical catalysts, did not exhibit any methane conversion at 500 °C and conversions on these materials did not light-off until above 550 °C (Fig. S6 in the Supplementary information).

In parallel experiments, consecutive 50 ppm SO<sub>2</sub>-aging treatments for periods of 30 min, 60 min or 120 min at 500 °C caused partial but irreversible deactivation of the Pd@CeO<sub>2</sub> and Pd@CZ samples (Fig. 4B). Conversely, the poisoning effect of SO<sub>2</sub> on Pd@ZrO<sub>2</sub> and Pd/Si-Al<sub>2</sub>O<sub>3</sub> catalysts was reversible at this temperature (Fig. 4B), even after 12 h aging (data not shown). Heating the Pd@ZrO<sub>2</sub> catalysts that had been aged at temperatures below 500 °C in dry conditions also resulted in complete reactivation of the materials. Finally, it should be noted that the conversion trends reported in Figs. 3 and 4B were affected by chromatographic effects due to the time required for the gas to flow through the catalytic system and to reach the analyzer. Therefore, the conversion at the beginning of reactivation can only be extrapolated.

At 600 °C, under dry conditions, methane was completely converted to CO<sub>2</sub> over all the catalysts and there was no loss of conversion during SO<sub>2</sub> exposure. To increase the sensitivity of the experiment, the catalysts were diluted by addition of Al<sub>2</sub>O<sub>3</sub> in a ratio of 1:3 and aged using the same conditions as those employed for the pure catalysts (Fig. 5). The diluted Pd@MO<sub>x</sub> catalysts all achieved complete conversion at 600 °C prior to SO<sub>2</sub> exposure, but the diluted Pd/Si-Al<sub>2</sub>O<sub>3</sub> catalyst showed only 80%

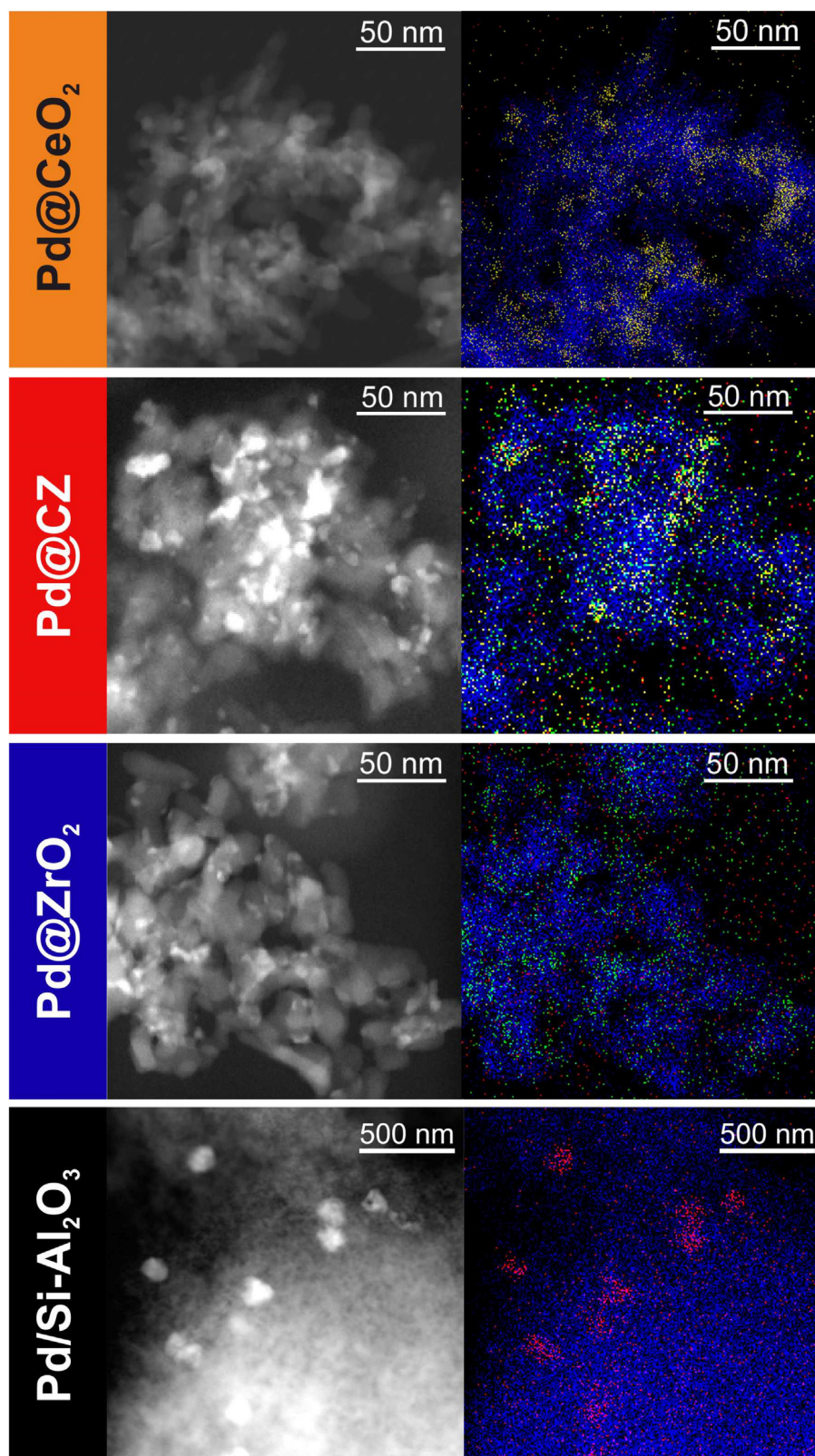


**Fig. 2.** Representative High-Angle Annular Dark-Field (HAADF) images (left column) and EDS mapping (right column) of samples Pd@CeO<sub>2</sub>/Si-Al<sub>2</sub>O<sub>3</sub> (Pd@CeO<sub>2</sub>), Pd@Ce<sub>0.6</sub>Zr<sub>0.4</sub>O<sub>2</sub>/Si-Al<sub>2</sub>O<sub>3</sub> (Pd@CZ), Pd@ZrO<sub>2</sub>/Si-Al<sub>2</sub>O<sub>3</sub> (Pd@ZrO<sub>2</sub>) and Pd/Si-Al<sub>2</sub>O<sub>3</sub>. EDS mapping colors: blue = Al, red = Pd, yellow = Ce, green = Zr. (For interpretation of the references to colour in this figure legend, the reader is referred to the web version of this article.)

conversion under these conditions. Exposure of the Pd@CeO<sub>2</sub> and Pd@CZ samples to SO<sub>2</sub> at this temperature caused the conversion to decrease continuously with time; however, for the Pd@ZrO<sub>2</sub> and

Pd/Si-Al<sub>2</sub>O<sub>3</sub> samples, after displaying an initially sharp decline in conversion, conversions partially recovered and reached a plateau value. This behavior was reproducible and was never observed for

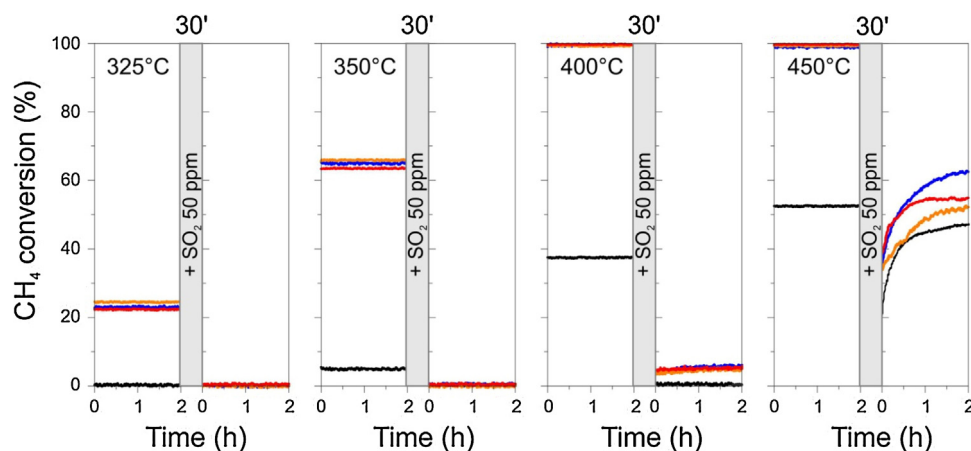


**Fig. 3.** Methane Catalytic oxidation: effect of 50 ppm  $\text{SO}_2$  dry aging for 30 min at different temperatures on the catalytic activity of Pd@CeO<sub>2</sub> (orange line), Pd@ZrO<sub>2</sub> (blue line), Pd@CZ (red line) and Pd/Si-Al<sub>2</sub>O<sub>3</sub> (black line). Conditions: 0.5% CH<sub>4</sub>; 2% O<sub>2</sub>; 50 ppm  $\text{SO}_2$  (if present) Ar balance, GHSV = 200000 mL g<sup>-1</sup> h<sup>-1</sup>. (For interpretation of the references to colour in this figure legend, the reader is referred to the web version of this article.)

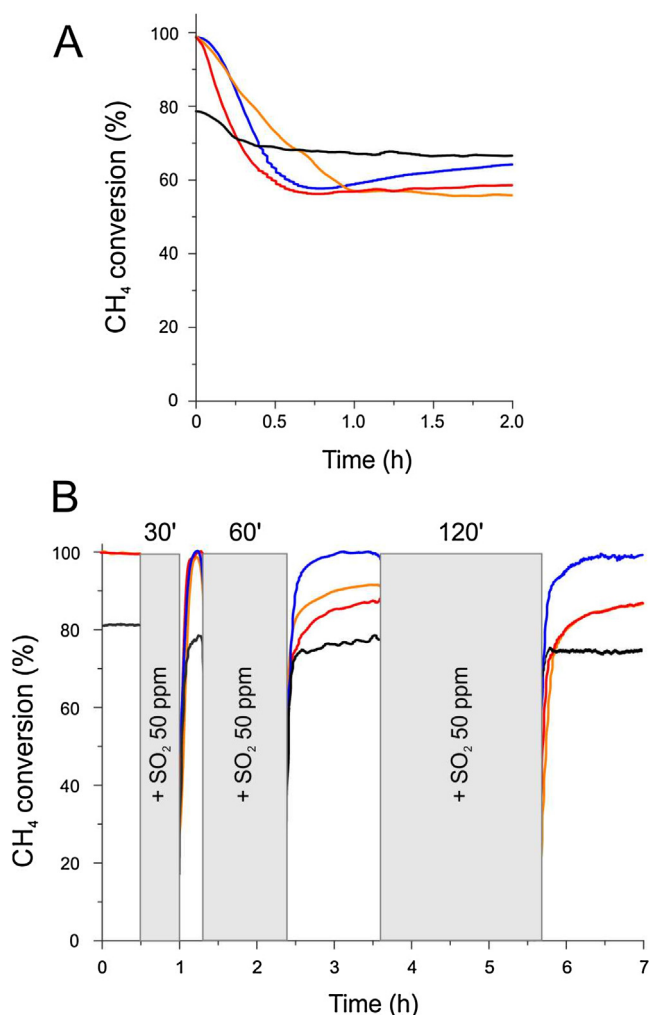


**Fig. 4.** Methane Catalytic oxidation: (A)  $\text{SO}_2$  dry aging at 500 °C. Pd@CeO<sub>2</sub> (orange line), Pd@ZrO<sub>2</sub> (blue line), Pd@CZ (red line) and Pd/Si-Al<sub>2</sub>O<sub>3</sub> (black line); (B) Reactivation trends following consecutive  $\text{SO}_2$  dry aging treatments at 500 °C. Conditions: 0.5% CH<sub>4</sub>; 2% O<sub>2</sub>; 50 ppm  $\text{SO}_2$  (if present) Ar balance, GHSV = 200000 mL g<sup>-1</sup> h<sup>-1</sup>. (For interpretation of the references to colour in this figure legend, the reader is referred to the web version of this article.)

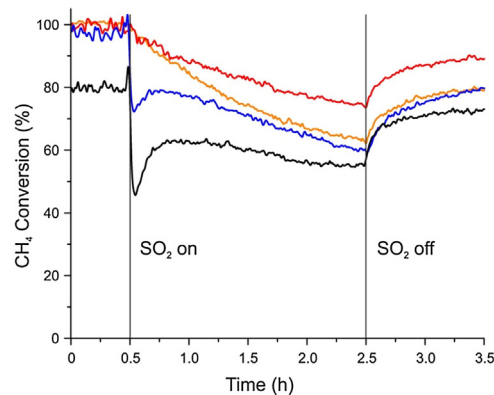


**Fig. 5.** Methane Catalytic Oxidation:  $\text{SO}_2$  dry aging at 600 °C and reactivation trends. Pd@CeO<sub>2</sub> (orange line), Pd@ZrO<sub>2</sub> (blue line), Pd@CZ (red line) and Pd/Si-Al<sub>2</sub>O<sub>3</sub> (black line). Conditions: 0.5% CH<sub>4</sub>; 2% O<sub>2</sub>; 50 ppm  $\text{SO}_2$  (if present) Ar balance, GHSV = 200000 mL g<sup>-1</sup> h<sup>-1</sup>. (For interpretation of the references to colour in this figure legend, the reader is referred to the web version of this article.)

CeO<sub>2</sub>-containing catalysts. A possible explanation for the transient behavior on Pd@ZrO<sub>2</sub> and Pd/Si-Al<sub>2</sub>O<sub>3</sub> is that  $\text{SO}_2$  initially deactivates the PdO active phase, competing with CH<sub>4</sub> for oxidation. Later,  $\text{SO}_3$  and sulfate species formed by oxidation migrate to the promoter/support. It has been previously reported that the activity of Pd/ZrO<sub>2</sub> catalysts can increase after  $\text{SO}_2$  aging due to formation of a composite site between PdO and sulfates at the PdO-support interface [39]. It is noteworthy that there was also an increase in conversion with  $\text{SO}_2$  exposure time at 500 °C for Pd@ZrO<sub>2</sub> and Pd@CZ catalysts (Fig. 4A), although the time scale for increasing conversion was much larger and the initial dip was not as sharp.

### 3.2. Model catalysts

The structure of the model catalysts used in this study is depicted graphically in Fig. 6A. A 1-mm thick quartz slide was used to support a 500-nm thick conductive layer of ITO, over which thin Al<sub>2</sub>O<sub>3</sub> layers were grown by ALD. The thickness of the Al<sub>2</sub>O<sub>3</sub> film was 5 nm, a value chosen so as to avoid both charging during XPS analysis and unwanted exposure of ITO after calcination (see SI for more information). To obtain a silanized, hydrophobic Si-Al<sub>2</sub>O<sub>3</sub> comparable to that of the HSA Si-Al<sub>2</sub>O<sub>3</sub>, the slides were allowed to react with TEOS by soaking them in TEOS solutions, diluted with toluene, for 2 days. Finally, the slides were loaded with Pd@CeO<sub>2</sub>, Pd@ZrO<sub>2</sub> or Pd@Ce<sub>0.6</sub>Zr<sub>0.4</sub>O<sub>2</sub> (Pd@CZ) particles and cal-



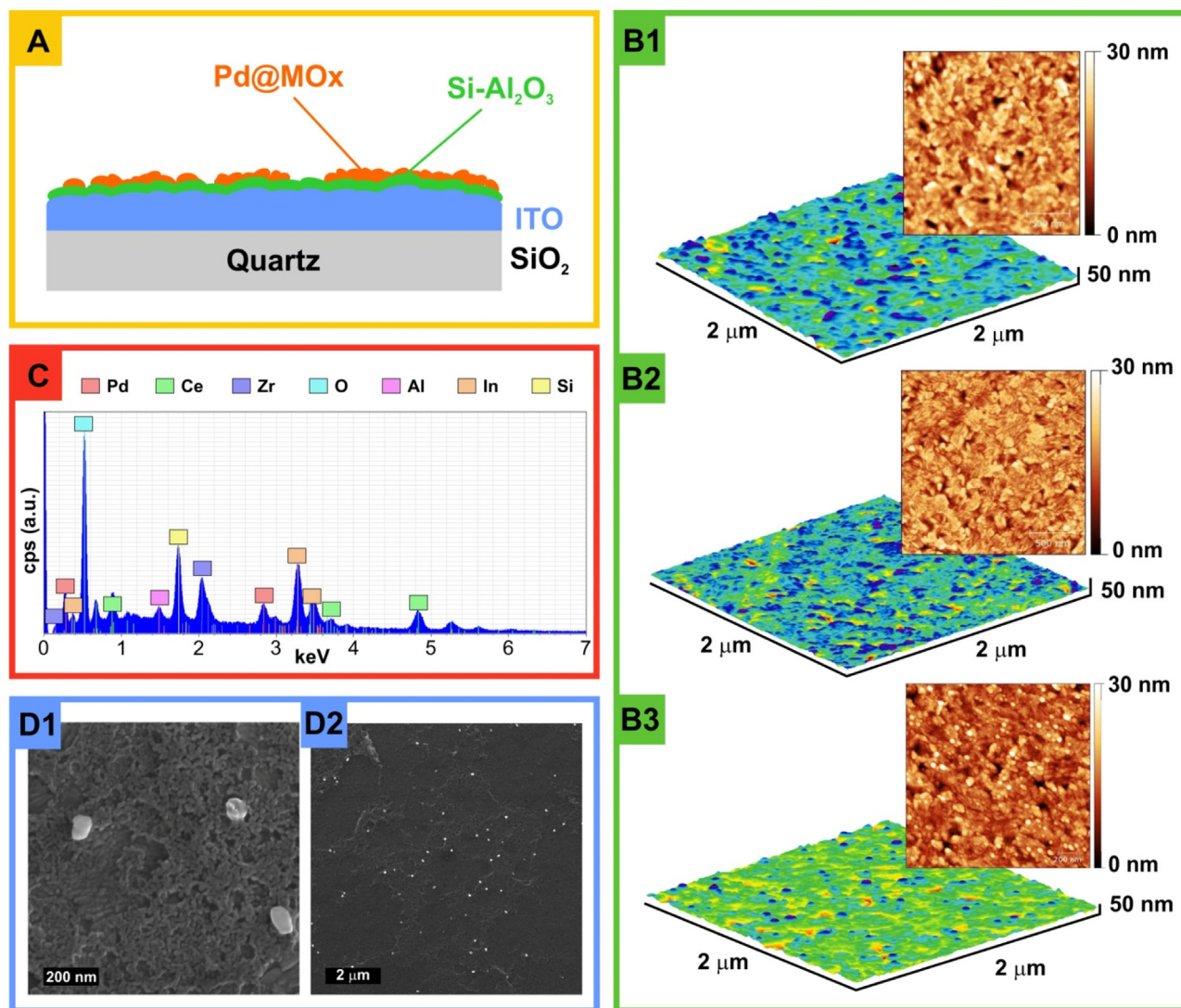


**Fig. 6.** Graphical representation of Pd@MO<sub>x</sub>/Si-Al<sub>2</sub>O<sub>3</sub>/ITO/quartz model (A, not to scale); AFM 3D image and mapping of ITO/quartz (B1), ALD-Al<sub>2</sub>O<sub>3</sub>/ITO/quartz (B2), Pd@CZ-m calcined at 850 °C for 5 h (B3). EDS wide spectrum of calcined Pd@CZ-m (C) and SEM image of Pd@CZ-m with 1 μm view field (D1) and 10 μm view field (D2).

cined at 850 °C for 5 h. The catalysts are labeled Pd@CeO<sub>2</sub>-m (m for model), Pd@ZrO<sub>2</sub>-m and Pd@CZ-m, respectively.

AFM analysis of the model catalysts was performed at different stages in the preparation procedure (Fig. 6B). The bare ITO surface shows characteristic worm-like structures (Fig. 6B1) which become slightly more defined in shape after Al<sub>2</sub>O<sub>3</sub> deposition (Fig. 6B2). The final structure obtained after depositing Pd@MO<sub>x</sub>, followed by calcination at 850 °C, shows a similar morphology, but with some aggregates on the surface (In Fig. 6B3, see the white spots in the 2D image, blue in the 3D image). Similar to the results reported in a recent paper by Zhang et al. [38], SEM/EDS analysis revealed aggregates composed of Pd with CeO<sub>2</sub>, ZrO<sub>2</sub> or CZ on top of small features that covered the Al<sub>2</sub>O<sub>3</sub> layer (Fig. 6D). A representative EDS spectrum of Pd@CZ-m is reported in Fig. 6C. The spectra obtained from different spots on the model catalysts revealed a uniform composition with the expected Pd:(Ce + Zr) and Ce:Zr molar ratio (1:5.5 and 6:4 respectively). CeO<sub>2</sub>- and ZrO<sub>2</sub>-based catalysts also showed the expected Pd:MO<sub>x</sub> molar ratio. No differences in surface morphology were observed for CeO<sub>2</sub>, ZrO<sub>2</sub> or CZ-containing samples.

Because the SRPES signals for Pd 3d and Zr 3p overlap (3p<sub>1/2</sub>: 343 eV, 3p<sub>3/2</sub>: 330 eV), only Pd 3d spectra of Pd@CeO<sub>2</sub>-m samples are reported here in Fig. 7. Calcination temperature had a significant effect on the Pd 3d region. Reference Pd@CeO<sub>2</sub>-m sam-

ples calcined at 500 °C showed the Pd spin-orbit split doublet (Pd 3d<sub>5/2</sub> and Pd 3d<sub>3/2</sub>) at 337.2 eV and 342.2 eV (Fig. 7A1), which can be assigned to PdO, based on previous XPS and X-ray Absorption Near Edge Structure (XANES) analysis of similar materials [40]. A shift of the PdO signal to higher BE (almost 1 eV) with respect to a bulk value is likely due to a size effect [41–47]. Calcination of the Pd@CeO<sub>2</sub>-m samples to 850 °C causes partial agglomeration of some of the nanostructures to form Pd and CeO<sub>2</sub> particles in the range of 50–100 nm (Fig. 7B2) [38]; and this agglomeration gives rise to an additional contribution in the Pd 3d spectra, more typical for bulk PdO (366.5 eV) (Fig. 7B2).

Because the relative contribution of the larger agglomerates in photoemission is expected to increase with excitation energy, we examined the surface:bulk signal contribution by tuning the SRPES excitation energy. In agreement with this, the signal at higher BE, tentatively assigned to PdO NPs, was relatively more intense at lower excitation energies, implying that this feature is associated with a considerably smaller structures. An alternative explanation is that the two contributions to the SRPES signal could be due to a Pd-Ce mixed oxide and a bulk PdO. For example, the Pd 3d signal of Pd-Ce mixed oxides has been reported to have BE of 338 eV BE [48]. Since the mixed oxides would likely segregate at higher temperatures, resulting in bulk PdO formation, this could also explain the

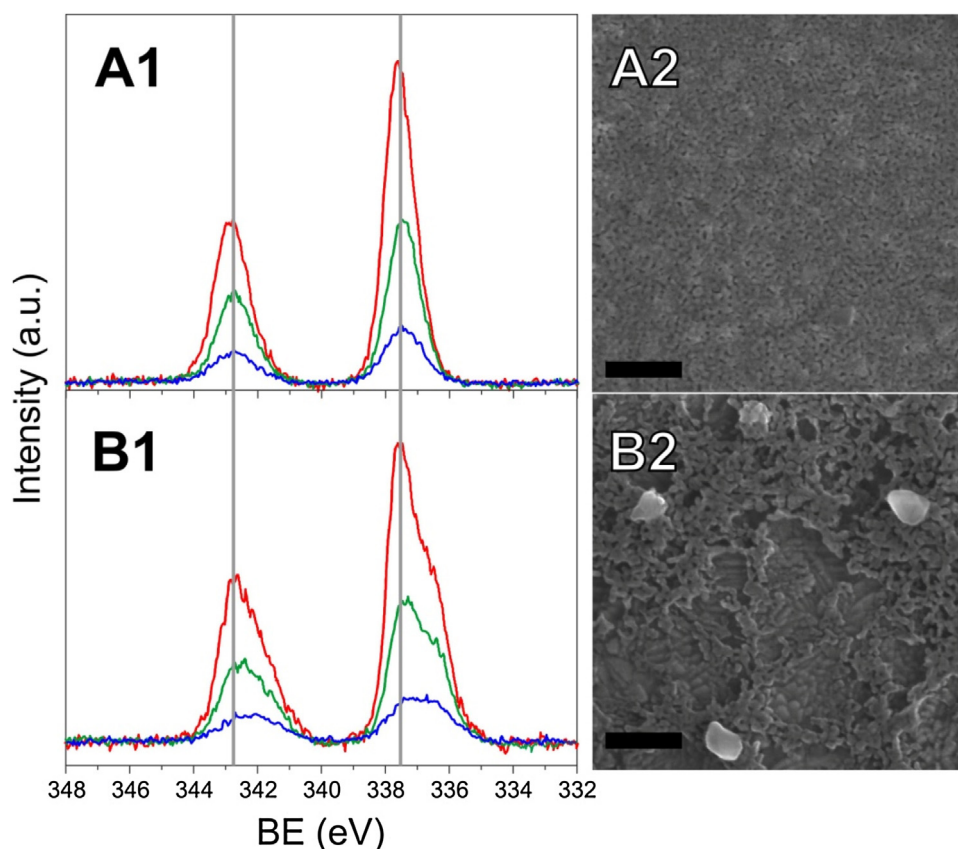


**Fig. 7.** Left: Pd 3d SRPES spectra at different excitation energies for Pd@CeO<sub>2</sub>-m calcined at 500 °C (A1) and 850 °C (B1). 500 eV: red line, 640 eV: green line, 880 eV: blue line. Grey lines are guidelines to the eye. Right: representative SEM images of Pd@CeO<sub>2</sub>-m samples calcined at 500 °C (A2) and 850 °C (B2); bars: 200 nm. (For interpretation of the references to colour in this figure legend, the reader is referred to the web version of this article.)

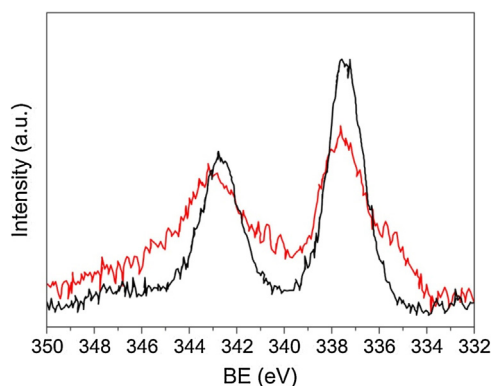


**Fig. 8.** XPS spectra of Pd 3d region of Pd@CeO<sub>2</sub>-m, fresh (black line) and 350 °C SO<sub>2</sub> aged (red line). (For interpretation of the references to colour in this figure legend, the reader is referred to the web version of this article.)

two features in the spectra [49]. However, we regard this explanation as less probable since the synthesis of the core-shell materials starts with pre-formed Pd nanoparticles and complete disruption of the PdO and incorporation into CeO<sub>2</sub> seems unlikely to occur at 500 °C. Also, this latter explanation does not agree with the observation of a PdO (101) reflection in the HSA catalysts calcined at 850 °C (Fig. 1) or with previous EXAFS studies on similar systems [11,40]. Due to the lower resolution, only one contribution averaging the signals associated to PdO NPs and aggregates was observed in XPS (Fig. 8).

In order to study the effect of SO<sub>2</sub> aging at different temperatures, the model catalysts were treated under similar conditions to

those used with the HSA catalysts (except for higher GHSV) and then transferred under inert atmosphere to the analysis chamber for analysis by XPS/SRPES. First, the catalysts were aged for 2 h under dry methane-oxidation (0.5% CH<sub>4</sub>, 2.0% O<sub>2</sub>) conditions with 50 ppm SO<sub>2</sub> at 350 °C, 500 °C or 600 °C. Then, after XPS analysis, the aged catalysts were regenerated under dry methane-oxidation conditions, without SO<sub>2</sub>, for 2 h at the same temperature at which they were aged. After SO<sub>2</sub> aging at 350 °C, the XPS spectrum showed a peak at 335.2 eV, which can be assigned to metallic Pd (Fig. 8) [20,50,51]. Partial reduction of PdO could result from SO<sub>2</sub> oxidation to SO<sub>3</sub> by PdO lattice oxygen. The complete re-oxidation of the then formed metallic Pd would not be possible under the conditions of this study at 350 °C, as previous XANES results on HSA Pd@CeO<sub>2</sub>/Si-Al<sub>2</sub>O<sub>3</sub> suggest, because of the low temperature and oxygen pressure involved [11]. A similar effect has been reported by Venezia et al. after aging Pd-based catalysts on TiO<sub>2</sub> or SiO<sub>2</sub> at the same temperature overnight [20,50] and by Liotta et al. for Pd/CeO<sub>2</sub> catalysts operated under lean conditions and 10 ppm of SO<sub>2</sub> [51].

Along with the reduction of the Pd, there was a slight increase of the XPS signal at higher BE following SO<sub>2</sub> aging at 350 °C. The shift of the signal is less than that expected for Pd in the form of PdSO<sub>4</sub> and we suggest that this might be indicative of some interaction with sulfates groups, in agreement with the literature [6,14]. After 2 h under dry methane-oxidation conditions at 350 °C, the XPS spectra did not change appreciably from those of the SO<sub>2</sub> aged catalyst. An irreversible poisoning of the PdO active phase would explain the similar behavior observed for HSA catalysts, regardless of the presence and composition of the promoter (Fig. 3). At higher temperature (500 °C to 600 °C) SRPES spectra of the Pd 3d region did not change after SO<sub>2</sub> aging or regeneration, suggesting that the interaction of PdO with sulfates is weaker and reversible. Accordingly, the



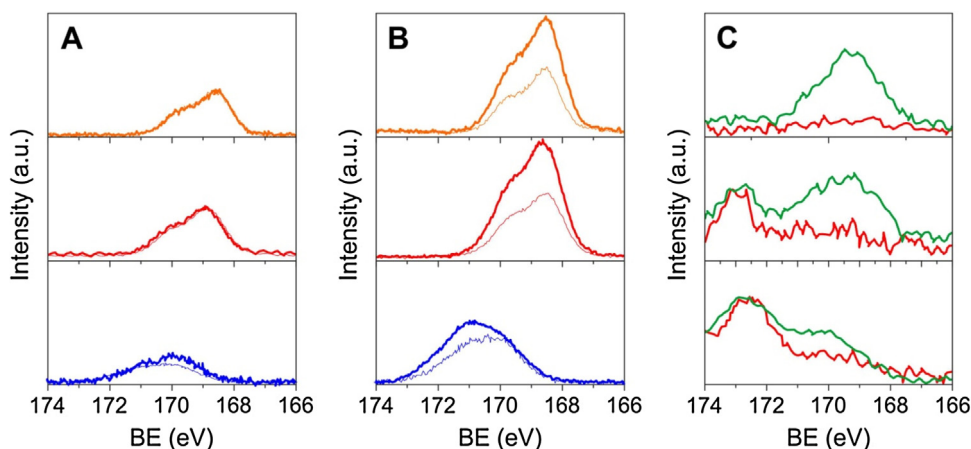


**Fig. 9.** S 2p region of SRPES spectra of SO<sub>2</sub> aged and regenerated samples at (A) 500 °C and (B) 600 °C (orange: Pd@CeO<sub>2</sub>-m; red: Pd@CZ-m; blue: Pd@ZrO<sub>2</sub>-m; thick line: aged; thin line: regenerated); (C) S 2p region of XPS spectra of SO<sub>2</sub> aged samples at 500 °C (red line) and 600 °C (green line) (top: Pd@CeO<sub>2</sub>-m; middle: Pd@CZ-m; bottom: Pd@ZrO<sub>2</sub>-m). (For interpretation of the references to colour in this figure legend, the reader is referred to the web version of this article.)

Pd/Si-Al<sub>2</sub>O<sub>3</sub> catalyst was very stable during dry SO<sub>2</sub> aging at 500 °C (Fig. 4A) and a sharp transient deactivation at 600 °C could only be observed on the diluted catalyst (Fig. 5). These observations are in accordance with thermodynamic calculations on PdSO<sub>4</sub> formation from mixtures of O<sub>2</sub> and SO<sub>3</sub>, predicting PdSO<sub>4</sub> decomposition below 400 °C [52].

Independent of the SO<sub>2</sub> aging temperature, the S 2p region of the SRPES/XPS spectra showed only a signal corresponding to sulfate species (168–172 eV BE). The use of SRPES was crucial in order to observe an intense and resolved S 2p signal, thanks to the much higher photoionization cross-section (0.83 Mbarn at 425 eV; 0.022 Mbarn at 1486.6 eV) [53] and shorter information length, which favors signal from surface species. Indeed, after 500 °C aging, sulfates were only observed in SRPES spectra and not in XPS spectra (Fig. 9A,C), which also showed an overlapping Zr 3d signal due to Al Kα<sub>3</sub> (1476.8 eV) and Kα<sub>4</sub> (1474.8 eV) lines. After 2 h of regeneration at 500 °C, sulfates were partially removed from Pd@ZrO<sub>2</sub>-m, while the sulfates remained on the Pd@CeO<sub>2</sub>-m and Pd@CZ-m samples, a finding consistent with the regeneration trends observed with the HSA catalysts (Fig. 4).

During regeneration of the catalyst, only a small fraction of sulfur species desorbed, suggesting that a rearrangement of sulfates on the surface could lead to reactivation and that TPD studies may give misleading results for evaluation of SO<sub>2</sub> poisoning resistance. At 600 °C, more sulfates are formed (even if a decrease in conversion was observed only in diluted samples) and these could be observed both in SRPES and XPS spectra (Fig. 9B,C). Based on the cross section corrected photoemission signal of S and Ce (and/or Zr) in XPS, we estimate a MO<sub>x</sub>:S molar ratio of 5:1 for CeO<sub>2</sub> and CZ and 7:1 for ZrO<sub>2</sub>. These ratios are consistent with about 1 monolayer (ML) of sulfate being formed on the surface of the oxide nanoparticles, considering that the XPS information depth is around 2 nm, which corresponds to about 6 ML of CeO<sub>2</sub> in the close-packed (111) direction. Regeneration under dry conditions at 600 °C resulted in desorption of sulfates from the surface/subsurface of all the samples (Fig. 9B), consistent with similar trends observed in the recovery of conversion (Fig. 5).

Previous FTIR [26], TPD [23] and XPS [54] studies reported sulfate desorption from Ce<sub>1</sub>Zr<sub>1-x</sub>O<sub>2</sub> in the range of 600 °C to 700 °C. The desorption of sulfate species from pure ZrO<sub>2</sub>-based materials is much less investigated, with TPD results showing higher desorption temperatures than for CeO<sub>2</sub> sulfates (800 °C) [23]. We suggest that the surface sensitivity of SRPES/XPS analysis allowed us to observe a partial desorption of sulfates from ZrO<sub>2</sub>, occurring at lower temperature, which could not be detected by TPD. The difference of

observed sulfate stability could also be due to the atmosphere in which desorption was performed, which can affect decomposition of S-species [17]. Indeed, Colussi et al. observed different TPD profiles on SO<sub>2</sub>-aged Pd/CeO<sub>2</sub>/Al<sub>2</sub>O<sub>3</sub> samples when the desorption was carried out in reaction conditions or inert atmosphere [17], suggesting a role of *in-situ* produced water in the SO<sub>2</sub> desorption mechanism.

Interestingly, the BE for the S 2p features in Fig. 9 was different for the Pd@CeO<sub>2</sub>-m and Pd@ZrO<sub>2</sub>-m samples, implying that sulfates bonded to Zr or Ce cations are distinguishable. Since the spectra of Pd@CZ-m are very similar to that of Pd@CeO<sub>2</sub> both in shape and formation/desorption trends, it appears that primarily Ce sulfates are formed on Pd@CZ-m samples and that these are similar to sulfates formed on CeO<sub>2</sub>. In agreement with this, the Ce 3d and Zr 3d XPS spectral regions show modifications after SO<sub>2</sub> aging that depend on the MO<sub>x</sub> composition (Fig. 10). In particular, Ce 3d spectra of Pd@CeO<sub>2</sub>-m (Fig. 10A) and Pd@CZ-m (Fig. 10C1) aged at 600 °C are similar and exhibit more intense Ce(III) contributions than what is observed on the fresh catalyst, probably due to reduction of CeO<sub>2</sub> by SO<sub>2</sub> with consequent formation of cerium sulfate. By contrast, Zr 3d spectra for Pd@ZrO<sub>2</sub>-m (Fig. 10B) are different from spectra for Pd@CZ-m (Fig. 10C2), revealing sulfate formation on Pd@ZrO<sub>2</sub>-m after aging at 500 °C and 600 °C, while the Pd@CZ-m spectra do not change. This is consistent with the formation of sulfates only on Ce cations in CZ materials, which leaves the chemical environment of Zr cations unaffected.

Fig. 11 shows the O 1s spectra of the fresh samples, exhibiting peaks typical of bulk oxygen (529 eV for CeO<sub>2</sub> and 531 eV for ZrO<sub>2</sub>) and hydroxyl species (532 eV) [55]. SO<sub>2</sub> aging leads to an increase in the intensity of the higher BE contribution (532 eV) associated with OH groups (Fig. 11). These results, taken together with the trends observed in S 2p spectra, suggest that the variation of O 1s signals is mostly due to oxygen from sulfate species.

#### 4. Discussion

First, the observations here demonstrate that the previously reported synthesis of Pd@CeO<sub>2</sub> and Pd@ZrO<sub>2</sub> particles by self-assembly can be extended to form materials with mixed-oxide shells, Pd@Ce<sub>x</sub>Zr<sub>1-x</sub>O<sub>2</sub>. The pre-formed core-shell particles can be deposited on both high-surface-area (HSA), functionalized alumina or on model Si-Al<sub>2</sub>O<sub>3</sub> surfaces to achieve a similar, controlled morphology. In all of the materials, the oxide shell was found to promote catalytic activity for methane oxidation. The series of hierarchically structured catalysts supported on Si-Al<sub>2</sub>O<sub>3</sub> also had

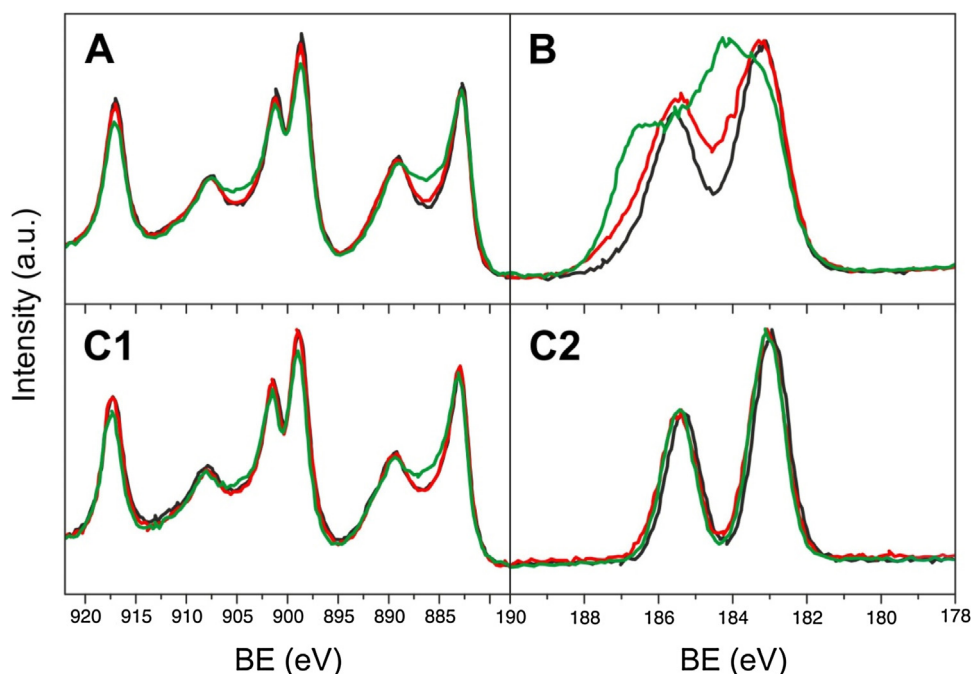


**Fig. 10.** XPS spectra of pristine samples (black line) and  $\text{SO}_2$  aged samples at  $500^\circ\text{C}$  (red line) and  $600^\circ\text{C}$  (green line). (A) Ce 3d region of  $\text{Pd@CeO}_2\text{-m}$ ; (B) Zr 3d region of  $\text{Pd@ZrO}_2\text{-m}$ ; (C1) Ce 3d region and (C2) Zr 3d region of  $\text{Pd@CZ-m}$ . (For interpretation of the references to colour in this figure legend, the reader is referred to the web version of this article.)

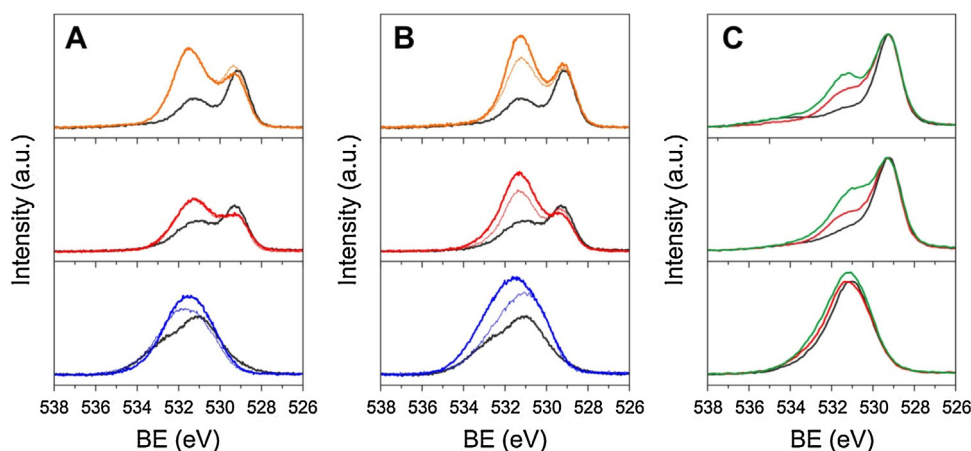


**Fig. 11.** O 1s region of SRPES spectra of  $\text{SO}_2$  aged and regenerated samples at (A)  $500^\circ\text{C}$  and (B)  $600^\circ\text{C}$  (orange:  $\text{Pd@CeO}_2\text{-m}$ ; red:  $\text{Pd@CZ-m}$ ; blue:  $\text{Pd@ZrO}_2\text{-m}$ ; thick line: aged; thin line: regenerated); (C) O 1s region of XPS spectra of  $\text{SO}_2$  aged samples at  $500^\circ\text{C}$  (red line) and  $600^\circ\text{C}$  (green line) (top:  $\text{Pd@CeO}_2\text{-m}$ ; middle:  $\text{Pd@CZ-m}$ ; bottom:  $\text{Pd@ZrO}_2\text{-m}$ ). SRPES and XPS spectra of fresh samples are reported for reference (black lines). (For interpretation of the references to colour in this figure legend, the reader is referred to the web version of this article.)

comparable surface areas and active-phase accessibilities. These properties make them good candidates to study the effect of the oxide promoter composition on  $\text{SO}_2$  poisoning.

The methods used in preparing the model catalysts in this study are also of general interest for investigating the effects of temperature and operating conditions. The approach is based on the ability of ALD to form uniform, thin films having precise thicknesses and a wide range of possible final compositions. Indeed, model supports could be prepared from almost any metal oxide by varying the ALD precursors [56]. This allows support composition to be varied systematically in order to study the effect of metal-support interactions on the catalyst performance, morphology (by SEM) and chemical state (by XPS/XANES). Also, model catalysts prepared in this way can be tested and analyzed repeatedly, making it possible to study the effect of aging and regeneration treatments together

with properties for adsorption, desorption or redistribution of surface species. The lower surface area of model catalysts, that affects the range of achievable GHSV, is the only drawback of this powerful method of investigation.

$\text{SO}_2$  poisoning of Pd-based catalysts in lean catalytic combustion of methane proceeds via two distinct mechanisms, depending on the aging temperature. At lower temperature ( $<450^\circ\text{C}$ ),  $\text{SO}_2$  irreversibly poisons PdO, causing a partial reduction to Pd and the formation of sulfates in close proximity to the active phase. The temperature is not high enough to allow the spillover of sulfate species from the active phase to the support/promoter and to promote a complete re-oxidation of the poisoned catalyst [11,57]. At higher temperatures, PdO is more resistant to poisoning, thanks to the spillover of sulfates from the active phase and/or the direct reaction of  $\text{SO}_2$  with the promoter. However, since the promoting

effect of the metal oxide is turned off by sulfate poisoning, the catalysts deactivate until a plateau is reached, corresponding to the active phase residual activity.

The effect of the oxide promoter composition on  $\text{SO}_2$  poisoning is also temperature dependent. At  $500^\circ\text{C}$ ,  $\text{Pd@ZrO}_2$  catalysts showed the best sulfur resistance among the samples, being only reversibly deactivated thanks to partial sulfate desorption. The performance of  $\text{Pd@CZ}$  catalysts is intermediate between that of the two pure oxides, suggesting that no cooperative effect of Ce and Zr takes place. On the other hand, at  $600^\circ\text{C}$ ,  $\text{Pd@CeO}_2$  and  $\text{Pd@CZ}$  can stabilize the catalyst against transient deactivation, acting as a sink for  $\text{SO}_2$ , while  $\text{Pd@ZrO}_2$  deactivates in a similar way as  $\text{Pd/Si-Al}_2\text{O}_3$ . However, the poisoning effect of  $\text{SO}_2$  is less relevant than at  $500^\circ\text{C}$ , since the deactivation is observed only for very high GHSV. These results make  $\text{Pd@ZrO}_2$  catalysts a more suitable candidate for real application, taking into account the better stability in the presence of  $\text{H}_2\text{O}$  with respect to  $\text{Pd@CeO}_2$  catalysts.

The chemical-state and surface sensitivity of photoelectron spectroscopy also allowed for the observation of preferential sulfation of Ce over Zr in CZ mixed oxides. The chemical environment of Zr cations only changed after sulfation of  $\text{ZrO}_2$ , while in the case of CZ no evident differences were observed. These results strongly suggest that sulfate species are associated with individual metal cations, producing a first evidence of what was tentatively proposed by Luo et al. based on TPD and pulse-reactor experiments [23].

## 5. Conclusions

The self-assembly methodology described previously [32] was modified in order to synthesize nanostructured  $\text{Pd@Ce}_x\text{Zr}_{1-x}\text{O}_2$  ( $\text{Pd@MO}_x$ ) units in the whole compositional range ( $0 < x < 1$ ). The synthesis of dispersed  $\text{Pd@MO}_x$  allowed the preparation of a series of high-surface-area  $\text{Si-Al}_2\text{O}_3$  supported catalysts and model catalysts having similar nanostructure and surface chemistry. Comparison of results on the two types of catalysts allowed the  $\text{SO}_2$  poisoning of methane oxidation on Pd-based catalysts to be systematically studied to elucidate the role of the  $\text{MO}_x$  promoter and the aging conditions. At lower temperatures ( $<450^\circ\text{C}$ ), the PdO active phase is irreversibly poisoned by  $\text{SO}_2$  due to interaction with sulfates which are not able to spillover to the support/promoter. At higher temperatures ( $>500^\circ\text{C}$ ), poisoning is slowed by formation of sulfate species on the oxide promoter. Due to partial decomposition of sulfates at  $500^\circ\text{C}$ ,  $\text{Pd@ZrO}_2$ -based catalysts showed the best sulfur-poisoning resistance, attaining complete regeneration even after prolonged aging, and thus they are the best candidates for real application.  $\text{Pd@Ce}_{0.6}\text{Zr}_{0.4}\text{O}_2$  catalysts showed intermediate sulfur tolerance compared to  $\text{Pd@CeO}_2$  and  $\text{Pd@ZrO}_2$ , in agreement with previously reported results [23]. The high chemical sensitivity of PES techniques provided direct evidence for previously suggested formation of sulfate species on individual metal cations in  $\text{Ce}_x\text{Zr}_{1-x}\text{O}_2$  mixed oxides [23]. Finally, the model-catalyst approaches developed here should allow the study of metal-support interactions in other catalytically relevant systems by simply varying the ALD-deposited thin film composition.

## Acknowledgments

The authors acknowledge CERIC-ERIC for open access to instrumentation and user support. This paper was also made possible by a NPRP Grant #6-290-1-059 from the Qatar National Research Fund (a member of Qatar Foundation). The statements made herein are solely the responsibility of the authors.

## Appendix A. Supplementary data

Supplementary data associated with this article can be found, in the online version, at <http://dx.doi.org/10.1016/j.apcatb.2016.09.016>.

## References

- [1] S.K. Matam, G.L. Chiarello, Y. Lu, A. Weidenkaff, D. Ferri, PdO x/Pd at work in a model three-way catalyst for methane abatement monitored by operando XANES, *Top. Catal.* 56 (2013) 239–242, <http://dx.doi.org/10.1007/s11244-013-9960-1>.
- [2] S. Colussi, A. Gayen, M.F. Camellone, M. Boaro, J. Llorca, S. Fabris, A. Trovarelli, Nanofaceted Pd-O sites in Pd-Ce surface superstructures: enhanced activity in catalytic combustion of methane, *Angew. Chem. Int. Ed.* 48 (2009) 8481–8484, <http://dx.doi.org/10.1002/anie.200903581>.
- [3] S. Colussi, C. De Leitenburg, G. Dolcetti, A. Trovarelli, The role of rare earth oxides as promoters and stabilizers in combustion catalysts, *J. Alloys Compd.* 374 (2004) 387–392, <http://dx.doi.org/10.1016/j.jallcom.2003.11.028>.
- [4] D. Ciuparu, M.R. Lyubovsky, E. Altman, L.D. Pfefferle, A. Datye, Catalytic combustion of methane over palladium-based catalysts, *Catal. Rev.* 44 (2002) 593–649, <http://dx.doi.org/10.1081/CR-120015482>.
- [5] W.R. Schwartz, L.D. Pfefferle, Combustion of methane over palladium-based catalysts: support interactions, *J. Phys. Chem. C* 116 (2012) 8571–8578, <http://dx.doi.org/10.1021/jp2119668>.
- [6] D.L. Mowery, R.L. McCormick, Deactivation of alumina supported and unsupported PdO methane oxidation catalyst: the effect of water on sulfate poisoning, *Appl. Catal. B Environ.* 34 (2001) 287–297, [http://dx.doi.org/10.1016/S0926-3373\(01\)00222-3](http://dx.doi.org/10.1016/S0926-3373(01)00222-3).
- [7] D. Ciuparu, L. Pfefferle, Support and water effects on palladium based methane combustion catalysts, *Appl. Catal. A Gen.* 209 (2001) 415–428, [http://dx.doi.org/10.1016/S0926-860X\(00\)00783-3](http://dx.doi.org/10.1016/S0926-860X(00)00783-3).
- [8] D. Ciuparu, N. Katsikis, L. Pfefferle, Temperature and time dependence of the water inhibition effect on supported palladium catalyst for methane combustion, *Appl. Catal. A Gen.* 216 (2001) 209–215, [http://dx.doi.org/10.1016/S0926-860X\(00\)00783-3](http://dx.doi.org/10.1016/S0926-860X(00)00783-3).
- [9] K. Persson, L.D. Pfefferle, W. Schwartz, A. Ersson, S.G. Järås, Stability of palladium-based catalysts during catalytic combustion of methane: the influence of water, *Appl. Catal. B Environ.* 74 (2007) 242–250, <http://dx.doi.org/10.1016/j.apcatb.2007.02.015>.
- [10] D. Ciuparu, E. Perkins, L. Pfefferle, In situ DR-FTIR investigation of surface hydroxyls on  $\gamma\text{-Al}_2\text{O}_3$  supported PdO catalysts during methane combustion, *Appl. Catal. A Gen.* 263 (2004) 145–153, <http://dx.doi.org/10.1016/j.apcata.2003.12.006>.
- [11] M. Monai, T. Montini, C. Chen, E. Fonda, R.J. Gorte, P. Fornasiero, Methane catalytic combustion over hierarchical  $\text{Pd@CeO}_2/\text{Si-Al}_2\text{O}_3$ : effect of the presence of water, *ChemCatChem* 7 (2015) 2038–2046, <http://dx.doi.org/10.1002/cctc.201402717>.
- [12] M. Honkane, M. Kärkkäinen, T. Kolli, O. Heikkinen, V. Viitanen, L. Zeng, H. Jiang, K. Kallinen, M. Huhtanen, R.L. Keiski, J. Lahtinen, E. Olsson, M. Vippola, Accelerated deactivation studies of the natural-gas oxidation catalyst-verifying the role of sulfur and elevated temperature in catalyst aging, *Appl. Catal. B Environ.* (2015), <http://dx.doi.org/10.1016/j.apcatb.2015.09.054>.
- [13] R.J. Farrauto, Low-temperature oxidation of methane, *Science* 337 (2012) 659–660, <http://dx.doi.org/10.1126/science.1226310>.
- [14] J. Lampert, M. Kazi, R. Farrauto, Palladium catalyst performance for methane emissions abatement from lean burn natural gas vehicles, *Appl. Catal. B Environ.* 14 (1997) 211–223, [http://dx.doi.org/10.1016/S0926-3373\(97\)00024-6](http://dx.doi.org/10.1016/S0926-3373(97)00024-6).
- [15] P. Gélin, L. Urfels, M. Primet, E. Tena, Complete oxidation of methane at low temperature over Pt and Pd catalysts for the abatement of lean-burn natural gas fuelled vehicles emissions: influence of water and sulphur containing compounds, *Catal. Today* 83 (2003) 45–57, [http://dx.doi.org/10.1016/S0920-5861\(03\)00215-3](http://dx.doi.org/10.1016/S0920-5861(03)00215-3).
- [16] United States Environmental Protection Agency, EPA420-F-06-064, 2006 <http://www.epa.gov/oms/highway-diesel/regs/420f06064.pdf>.
- [17] S. Colussi, F. Arosio, T. Montanari, G. Busca, G. Groppi, A. Trovarelli, Study of sulfur poisoning on  $\text{Pd/Al}_2\text{O}_3$  and  $\text{Pd/CeO}_2/\text{Al}_2\text{O}_3$  methane combustion catalysts, *Catal. Today* 155 (2010) 59–65, <http://dx.doi.org/10.1016/j.cattod.2009.02.019>.
- [18] P. Gélin, M. Primet, Complete oxidation of methane at low temperature over noble metal based catalysts: a review, *Appl. Catal. B Environ.* 39 (2002) 1–37, [http://dx.doi.org/10.1016/S0926-3373\(02\)00076-0](http://dx.doi.org/10.1016/S0926-3373(02)00076-0).
- [19] T. Luo, J.M. Vohs, R.J. Gorte, An examination of sulfur poisoning on Pd/Ceria catalysts, *J. Catal.* 210 (2002) 397–404, <http://dx.doi.org/10.1006/jcat.2002.3689>.
- [20] A.M. Venezia, G. Di Carlo, G. Pantaleo, L.F. Liotta, G. Melaeet, N. Kruse, Oxidation of  $\text{CH}_4$  over Pd supported on  $\text{TiO}_2$ -doped  $\text{SiO}_2$ : effect of Ti(IV) loading and influence of  $\text{SO}_2$ , *Appl. Catal. B Environ.* 88 (2009) 430–437, <http://dx.doi.org/10.1016/j.apcatb.2008.10.023>.



- [21] J.A. Rodriguez, T. Jirsak, A. Freitag, J.C. Hanson, J.Z. Larese, S. Chaturvedi, Interaction of SO<sub>2</sub> with CeO<sub>2</sub> and Cu/CeO<sub>2</sub> catalysts: photoemission, XANES and TPD studies, *Catal. Lett.* 62 (1999) 113–119, ISI: 000083512000005.
- [22] P. Bazin, O. Saur, J.C. Lavalley, G. Blanchard, V. Visciglio, O. Touret, Influence of platinum on ceria sulfation, *Appl. Catal. B Environ.* 13 (1997) 265–274.
- [23] T. Luo, R.J. Gorte, Characterization of SO<sub>2</sub>-poisoned ceria-zirconia mixed oxides, *Appl. Catal. B Environ.* 53 (2004) 77–85, <http://dx.doi.org/10.1016/j.apcatb.2004.04.020>.
- [24] E.J. Romano, K.H. Schulz, A XPS investigation of SO<sub>2</sub> adsorption on ceria-zirconia mixed-metal oxides, *Appl. Surf. Sci.* 246 (2005) 262–270, <http://dx.doi.org/10.1016/j.apsusc.2004.11.017>.
- [25] S. Deshmukh, M. Zhang, V.I. Kovalchuk, J.L. d'Itri, Effect of SO<sub>2</sub> on CO and C<sub>3</sub>H<sub>8</sub> oxidation over CeO<sub>2</sub> and Ce<sub>0.75</sub>Zr<sub>0.25</sub>O<sub>2</sub>, *Appl. Catal. B Environ.* 45 (2003) 135–145, [http://dx.doi.org/10.1016/S0926-3373\(03\)00128-0](http://dx.doi.org/10.1016/S0926-3373(03)00128-0).
- [26] M. Waqif, P. Bazin, O. Saur, J.C. Lavalley, G. Blanchard, O. Touret, Study of ceria sulfation, *Appl. Catal. B Environ.* 11 (1997) 193–205, [http://dx.doi.org/10.1016/S0926-3373\(96\)00040-9](http://dx.doi.org/10.1016/S0926-3373(96)00040-9).
- [27] M. Cargnello, V.V.T. Doan-Nguyen, T.R. Gordon, R.E. Diaz, E.A. Stach, R.J. Gorte, P. Fornasiero, C.B. Murray, Control of metal nanocrystal size reveals metal-support interface role for ceria catalysts, *Science* 341 (2013) 771–773, <http://dx.doi.org/10.1126/science.1224048>.
- [28] M. Cargnello, J.J.D. Jaen, J.C.H. Garrido, K. Bakhmutsky, T. Montini, J.J.C. Gamez, R.J. Gorte, P. Fornasiero, Exceptional activity for methane combustion over modular Pd@CeO<sub>2</sub> subunits on functionalized Al<sub>2</sub>O<sub>3</sub>, *Science* 337 (2012) 713–717, <http://dx.doi.org/10.1126/science.1222887>.
- [29] C. Chen, Y.-H. Yeh, M. Cargnello, C.B. Murray, P. Fornasiero, R.J. Gorte, Methane oxidation on Pd@ZrO<sub>2</sub>/Si–Al<sub>2</sub>O<sub>3</sub> is enhanced by surface reduction of ZrO<sub>2</sub>, *ACS Catal.* 4 (2014) 3902–3909, <http://dx.doi.org/10.1021/cs501146u>.
- [30] K. Bakhmutsky, N.L. Wieder, M. Cargnello, B. Galloway, P. Fornasiero, R.J. Gorte, A versatile route to core-shell catalysts: synthesis of dispersible M@oxide (M = Pd, Pt; oxide = TiO<sub>2</sub>, ZrO<sub>2</sub>) nanostructures by self-assembly, *ChemSusChem* 5 (2012) 140–148, <http://dx.doi.org/10.1002/cssc.201100491>.
- [31] A.E. Nelson, K.H. Schulz, Surface chemistry and microstructural analysis of Ce<sub>x</sub>Zr<sub>1-x</sub>O<sub>2-y</sub> model catalyst surfaces, *Appl. Surf. Sci.* 210 (2003) 206–221, [http://dx.doi.org/10.1016/S0169-4332\(03\)00157-0](http://dx.doi.org/10.1016/S0169-4332(03)00157-0).
- [32] M. Cargnello, N.L. Wieder, P. Canton, T. Montini, G. Giambastiani, A. Benedetti, R.J. Gorte, P. Fornasiero, A versatile approach to the synthesis of functionalized thiol-protected palladium nanoparticles, *Chem. Mater.* 23 (2011) 3961–3969, <http://dx.doi.org/10.1021/cm2014658>.
- [33] L. Adjianto, D.A. Bennett, C. Chen, A.S. Yu, M. Cargnello, P. Fornasiero, R.J. Gorte, J.M. Vohs, Exceptional thermal stability of Pd@CeO<sub>2</sub> core-shell catalyst nanostructures grafted onto an oxide surface, *Nano Lett.* 13 (2013) 2252–2257, <http://dx.doi.org/10.1021/nl4008216>.
- [34] T. Skála, F. Šutara, K.C. Prince, V. Matolín, Cerium oxide stoichiometry alteration via Sn deposition: influence of temperature, *J. Electron. Spectrosc. Relat. Phenom.* 169 (2009) 20–25, <http://dx.doi.org/10.1016/j.elspec.2008.10.003>.
- [35] R.S. Zhou, R.L. Snyder, Structures and transformation mechanisms of the  $\eta$ ,  $\gamma$  and  $\theta$  transition aluminas, *Acta Crystallogr. Sect. B Struct. Sci.* (1991) 617–630, <http://dx.doi.org/10.1107/S0108768191002719>.
- [36] G. Colón, F. Valdivieso, M. Pijolat, R.T. Baker, J.J. Calvino, S. Bernal, Textural and phase stability of Ce<sub>x</sub>Zr<sub>1-x</sub>O<sub>2</sub> mixed oxides under high temperature oxidising conditions, *Catal. Today* 50 (1999) 271–284, [http://dx.doi.org/10.1016/S0920-5861\(98\)00509-4](http://dx.doi.org/10.1016/S0920-5861(98)00509-4).
- [37] T. Montini, M. Melchionna, M. Monai, P. Fornasiero, Fundamentals and catalytic applications of CeO<sub>2</sub>-based materials, *Chem. Rev.* (2016), <http://dx.doi.org/10.1021/acs.chemrev.5b00603>.
- [38] S. Zhang, C. Chen, M. Cargnello, P. Fornasiero, R.J. Gorte, G.W. Graham, Xiaoqing Pan, Dynamic structural evolution of supported palladium-ceria core-shell catalysts revealed by in situ electron microscopy, *Nat. Commun.* 6 (2015), <http://dx.doi.org/10.1038/ncomms8778>.
- [39] R. Burch, D.J. Crittle, B.W.L. Southward, J.A. Sullivan, The effect of SO<sub>2</sub> on the activity of Pd-based catalysts in methane combustion, *Catal. Lett.* 72 (2001) 153–155, <http://dx.doi.org/10.1023/A:1009088112345>.
- [40] M. Monai, T. Montini, M. Melchionna, T. Duchoň, P. Kúš, N. Tsud, K.C. Prince, V. Matolín, R.J. Gorte, P. Fornasiero, Phosphorus poisoning during wet oxidation of methane over Pd@CeO<sub>2</sub>/graphite model catalysts, *Appl. Catal. B Environ.* (2015), <http://dx.doi.org/10.1016/j.apcatb.2015.10.001>.
- [41] H. He, C. Gao, A general strategy for the preparation of carbon nanotubes and graphene oxide decorated with PdO nanoparticles in water, *Molecules* 15 (2010) 4679–4694, <http://dx.doi.org/10.3390/molecules15074679>.
- [42] P. Zhang, T.K. Sham, X-Ray studies of the structure and electronic behavior of alkanethiolate-capped gold nanoparticles: the interplay of size and surface effects, *Phys. Rev. Lett.* 90 (2003) 245502, <http://dx.doi.org/10.1103/PhysRevLett.90.245502>.
- [43] J. Morales, J.P. Espinos, A. Caballero, A.R. Gonzalez-Elipé, J.A. Mejías, XPS study of interface and ligand effects in supported Cu<sub>2</sub>O and CuO nanometric particles, *J. Phys. Chem. B* 109 (2005) 7758–7765, <http://dx.doi.org/10.1021/jp0453055>.
- [44] V. Johánek, I. Stará, N. Tsud, K. Veltruská, V. Matolín, CO adsorption on Al<sub>2</sub>O<sub>3</sub>-supported Pd clusters: XPS study, *Appl. Surf. Sci.* 162 (2000) 679–684.
- [45] H.-F. Wang, W.E. Kaden, R. Dowler, M. Sterrer, H.-J. Freund, Model oxide-supported metal catalysts – comparison of ultrahigh vacuum and solution based preparation of Pd nanoparticles on a single-crystalline oxide substrate, *Phys. Chem. Chem. Phys.* 14 (2012) 11525–11533, <http://dx.doi.org/10.1039/C2CP41459G>.
- [46] S. Penner, P. Bera, S. Pedersen, L.T. Ngo, J.J.W. Harris, C.T. Campbell, Interactions of O<sub>2</sub> with Pd nanoparticles on  $\alpha$ -Al<sub>2</sub>O<sub>3</sub>(0001) at low and high O<sub>2</sub> pressures, *J. Phys. Chem. B* 110 (2006) 24577–24584, <http://dx.doi.org/10.1021/jp0630267>.
- [47] R. Lin, R.G. Freemantle, N.M. Kelly, T.R. Fielitz, S.O. Obare, R.Y. Ofoli, In situ immobilization of palladium nanoparticles in microfluidic reactors and assessment of their catalytic activity, *Nanotechnology* 20 (2010) 325605, <http://dx.doi.org/10.1088/0957-4484/21/32/325605>.
- [48] K.R. Priolkar, P. Bera, P.R. Sarode, M.S. Hegde, S. Emura, R. Kumashiro, N.P. Lalla, Formation of Ce<sub>1-x</sub>Pd<sub>x</sub>O<sub>2-δ</sub> solid solution in combustion-synthesized Pd/CeO<sub>2</sub> catalyst: XRD, XPS, and EXAFS investigation, *Chem. Mater.* 14 (2002) 2120–2128, <http://dx.doi.org/10.1021/cm0103895>.
- [49] C.I. Hiley, J.M. Fisher, D. Thompson, R.J. Kashtiban, J. Sloan, R.I. Walton, Incorporation of square-planar Pd<sup>2+</sup> in fluorite CeO<sub>2</sub>: hydrothermal preparation, local structure, redox properties and stability, *J. Mater. Chem. A* 3 (2015) 13072–13079, <http://dx.doi.org/10.1039/C5TA02007G>.
- [50] A.M. Venezia, R. Murania, G. Pantaleo, G. Deganello, Pd and PdAu on mesoporous silica for methane oxidation: effect of SO<sub>2</sub>, *J. Catal.* 251 (2007) 94–102, <http://dx.doi.org/10.1016/j.jcat.2007.07.013>.
- [51] L.F. Liotta, G. DiCarlo, G. Pantaleo, A.M. Venezia, G. Deganello, Insights into SO<sub>2</sub> interaction with Pd/Co<sub>3</sub>O<sub>4</sub>-CeO<sub>2</sub> catalysts for methane oxidation, *Top. Catal.* 52 (2009) 1989–1994, <http://dx.doi.org/10.1007/s11244-009-9375-1>.
- [52] H.N. Sharma, V. Sharma, A.B. Mhadeshwar, R. Ramprasad, Why Pt survives but Pd suffers from SO<sub>x</sub> poisoning? *J. Phys. Chem. Lett.* 6 (2015) 1140–1148, <http://dx.doi.org/10.1021/jz5027147>.
- [53] J.J. Yeh, I. Lindau, Atomic subshell photoionization cross sections and asymmetry parameters: 1 < Z < 103, *At. Data Nucl. Data Tables* 32 (1985) 1–155, [http://dx.doi.org/10.1016/0092-640X\(85\)90016-6](http://dx.doi.org/10.1016/0092-640X(85)90016-6).
- [54] R.M. Ferrizz, R.J. Gorte, J.M. Vohs, TPD and XPS investigation of the interaction of SO<sub>2</sub> with model ceria catalysts, *Catal. Lett.* 82 (2002) 123–129, <http://dx.doi.org/10.1023/A:1020512713021>.
- [55] D.R. Mullins, P.M. Albrecht, T.-L. Chen, F.C. Calaza, M.D. Biegalski, H.M. Christen, S.H. Overbury, Water dissociation on CeO<sub>2</sub>(100) and CeO<sub>2</sub>(111) thin films, *J. Phys. Chem. C* 116 (2012) 19419–19428, <http://dx.doi.org/10.1021/jp306444h>.
- [56] B.J. O'Neill, D.H.K. Jackson, J. Lee, C. Canlas, P.C. Stair, C.L. Marshall, J.W. Elam, T.F. Kuech, J.A. Dumesic, G.W. Huber, Catalyst design with atomic layer deposition, *ACS Catal.* 5 (2015) 1804–1825, <http://dx.doi.org/10.1021/cs501862h>.
- [57] R. Burch, F.J. Urbano, Investigation of the active state of supported palladium catalysts in the combustion of methane, *Appl. Catal. A Gen.* 124 (1995) 121–138, [http://dx.doi.org/10.1016/0926-860X\(94\)00252-5](http://dx.doi.org/10.1016/0926-860X(94)00252-5).